Supplementary Information

Synergy of Fe dopants and oxygen vacancies confined in atomically-thin cobaltous oxide sheets for high-efficiency CO_2 photoreduction

Kui Chen[a,b,#], Sheng Zhou[a,#], Tongtong Jiang[a,*], Xiaodong Li[b], Jing Yu[b], Qiuyan Wang[b], Xiaoliang Xu[b,*] and Lixin Zhu[c,*]

[a] *Information Materials and Intelligent Sensing Laboratory of Anhui Province, Anhui University, 230601 Hefei, China;*

[b] *Key Laboratory of Strongly-Coupled Quantum Matter Physics, Chinese Academy of Sciences， School of Physical Sciences， University of Science and Technology of China, Hefei Anhui 230026, P.R. China;*

[c] *Department of General Surgery & Central Laboratory, the First Affiliated Hospital of Anhui Medical University, Hefei Anhui 230022, P.R. China.*

Experimental Section

Chemicals: $C_{15}H_{21}FeO_6$ (Iron(III) acetylacetonate, 98%), $C_{15}H_{21}CoO_6$ (Cobalt acetylacetonate, 98%) were purchased from Aladdin Reagent (Shanghai) Co., Ltd; CTAB (Hexadecyl trimethyl ammonium bromide,AR), $C_2H_6O_2$ (Ethylene glycol, AR), and C_2H_6O (ethanol, AR) were provided from Shanghai Chemical Reagent Factory. Above reagents were without further purification. Millipore water of resistivity of 18.2 MΩ·cm was used in the whole experimental process.

Synthesis of Fe-Co based nanosheets precursors: Fe-Co based nanosheets were synthesized by hydrothermal and annealing treatment. First, 600 mg $C_{15}H_{21}CoO_6$ was dispersed in the solution with 60 mL $C_2H_6O_2$ and 11 mL H_2O containing 2.2 g CTAB. Then, 30 mg $C_{15}H_{21}FeO_6$ was added to above homogeneous solution under stirring, followed by transferring the solution into the polytetrafluoroethylene (PTFE) lining and disposing under 180 °C for 48 h. Fe-Co based nanosheets precursors were obtained by collecting, washing and drying. Co based nanosheets precursors were prepared in the same way except that no $C_{15}H_{21}FeO_6$ was added.

Synthesis of Fe-Co based single-unit-cell layers: Fe-Co based nanosheets precursors were placed in a quartz box under the annealing environment of 50 Pa pressure. Next, the precursors were heated up to 350 °C with 10 °C s^{-1} heating rate, and holded for 5 min, then took out the sample immediately when time was up. The obtained samples were referred as V_o-Fe-CoO single-unit-cell layers. And Fe-CoO single-unit-cell layers were prepared in similar experimental procedures under 100 Pa and with 2.5 L min^{-1} of air flow rate for annealing. V_o-CoO and CoO single-unit-cell layers were obtained with the same rapid annealing procedure using Co based nanosheets precursors.

By heat treatment at high temperature in a certain atmosphere can introduces oxygen vacancies. According to interequilibrium principle of the oxygen at the contact interface of two phases and standard Kröger-Vink notation, the formation of oxygen vacancies at high temperatures follows the following equilibrium:

$$O_O \leftrightharpoons V_O + 1/2\ O_2(g) + 2e^-$$

The equilibrium constant K for this reaction can be expressed as

$$K = [V_o]n^2\ p(O_2)^{1/2}$$

The above equation can be transformed into

$$[V_o] = Kn^{-2}\ p(O_2)^{-1/2}$$

Where O_o represent the lattice oxygen, V_O is oxygen vacancy. $[V_o]$ denotes the concentration of oxygen vacancies,

n denotes the concentration of electrons, $p(O_2)$ is oxygen pressure. Oxygen vacancy concentration decreases with increasing oxygen partial pressure. Therefore, high temperature heat treatment under hypoxic conditions is beneficial to the formation of oxygen vacancy. Therefore, under vaccum condition, the sample with abundant oxygen vacancies were obtained, but under Air condition of 100 Pa, the increasement of oxygen pressure induce the reduction of oxygen vacancies.[1,2]

Materials characterization

The morphology and corresponding element analysis of samples were explored by a JEOL JEM-ARM200F TEM/STEM with a spherical aberration corrector. XRD patterns were recorded using an X-ray diffractometer (XRD Bruker D8-ADVANCE) with Cu Ka radiation (λ=0.15406 nm). AFM measurements were conducted using an Atomic Force Microscopy (AFM5500M). The surface information of elemental was characterized by X-ray photoelectron spectroscopy (XPS, ESCALAB 250Xi). Various reaction intermediates in the CO_2 reduction process were measured using In-situ Fourier-transform infrared spectroscopy (FTIR, Thermo Scientific Nicolet iS50 Set-up).

Photocatalytic CO_2 reduction measurements: The photocatalytic reduction CO_2 measurement were carried out in the all-glass automatic online trace gas analysis system (Beijing China PerfectLight, Labsolar -6A). In the CO_2 photocatalytic process, the 18 mg sample is evenly dispersed on a quartz disc with a radius of 3cm, then the quartz plate and 10 mL deionized water were sealed in the 560 ml quartz reactor. After the quartz reactor was connected to Labsolar -6A, the reaction system was vacuumed and scrubbed by CO_2. Next, the system is kept at 80 Pa CO_2 pressure for 1h to stabilize, then turn on the light for CO_2 reduction test. Light irradiation was provided by a MC-XF300 Xe lamp (Beijing MerryChange Technology CO., LTD.) with a standard AM 1.5G filter for simulating visible light, with an output light density of ~950 mW cm^{-2}, and the system had been working at a temperature of 298±0.2 K. The products of the CO_2 reduction process were periodically detected by analyzing chromatographic peaks from the gas chromatography (Techcomp GC7900 gas chromatograph, FID detector, TDX-01 column)

Photoelectrochemical measurements: Related electrochemical tests were completed with the CHI760E electrochemical workstation (CH Instruments Ins). 0.5 M Na_2SO_4 solution was used for the photocurrent density spectra and Mott−Schottky measurements. The mixed solution containing 0.1 M $K_3[Fe(CN)_6]$, 0.1 M $K_4Fe(CN)_6$ and 0.1 M KCl was used in EIS measurements. The measurement was conducted with a conventional three electrodes cell using the Pt as the counter electrode, saturated calomel electrode as the reference electrode, and a 2.2 cm×2.2 cm FTO coated with 4 mg sample and 15 μL Nafion as working electrodes.

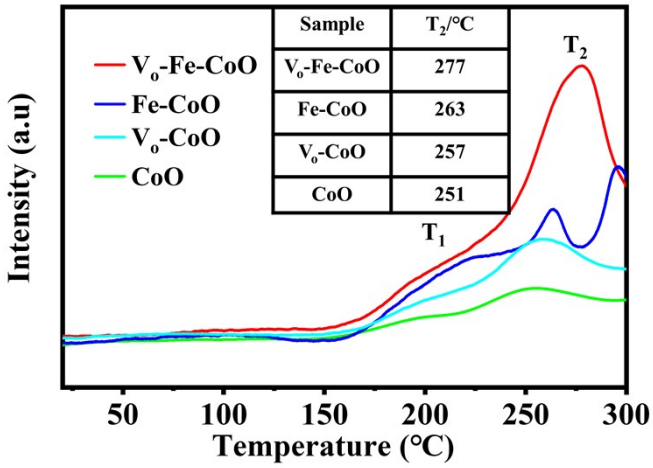

Fig. S1 CO_2 temperature-programmed desorption (CO_2-TPD) of V_o-Fe-CoO, Fe-CoO, V_o-CoO and CoO single-unit-cell layers.

CO_2 temperature-programmed desorption (CO_2-TPD) was conduct to explore CO_2 adsorption properties of samples. In Fig.S1, the weak desorption peaks around 180 °C (T_1) correspond with the weak adsorption for CO_2 related to the surface hydroxyl group.[3] In addition, the desorption temperature of CO_2 from the metal sites (T_2 in Fig. S1) ranges from 150°C to 280 °C,[24] and the desorption temperature of CO_2 from samples increased order CoO < V_o-CoO < Fe-CoO < V_o-Fe-CoO. The shift to higher temperature of T_2 demonstrates the increase in the strength of basic sites corresponding stronger CO_2 activation ability.[5,6] These results are consistent with CO_2 absorption energy barriers of samples displayed in Fig. 5f.

First-principles Calculations

All the calculations were carried out by using Vienna Ab initio Simulation Package (VASP) based on density functional theory (DFT) using projector augmented wave (PAW) potentials. The exchange-correlation between electrons was treated using the generalized gradient approximation (GGA) of Perdew-Becke-Ernzerhof (PBE).[5,6] To achieve the accuracy of the calculated results, the plane wave cutoff energy was set to 480 eV. A Monkhorst-Pack 3×3×1 k-point grid was used to sample the Brillouin zone. All structures were optimized under the conventional energy (10^{-4} eV) and force (0.02 eV/Å) convergence criteria.

Gibbs free energies for the adsorbed intermediates were calculated at 298.15 K according to the following equation:

$$G = E_{DFT} + E_{ZPE} - T\Delta S \quad (S1)$$

E_{DFT} is the electronic energy calculated with VASP. E_{ZPE}, and TΔS are the free energy from zero-point vibration energy, and entropy, respectively.

In this paper, the obtained free energy changes were presented as following:

$$G[H^+ + e^-] = 0.5 \times G[H_2] - eU \quad (S2)$$

$$\Delta G[*COOH] = G[*COOH] + 7\times G[H^+ + e^-] - (G[*] + G[CO_2] + 8\,G[H^+ + e^-]) \quad (S3)$$

$$\Delta G[*CO] = G[*CO] + G[H_2O] + 6 \times G[H^+ + e^-] - (G[*] + G[CO_2] + 8\,G[H^+ + e^-]) \quad (S4)$$

$$\Delta G[*+CO] = G[*] + G[CO] + G[H_2O] + 6 \times G[H^+ + e^-] - (G[*] + [CO_2] + 8\,G[H^+ + e^-]) \quad (S5)$$

$$\Delta G[*CHO] = G[*CHO] + G[H_2O] + 5 \times G[H^+ + e^-] - (G[*] + G[CO_2] + 8\,G[H^+ + e^-]) \quad (S6)$$

$$\Delta G[*CH_2O] = G[*CH_2O] + G[H_2O] + 4 \times G[H^+ + e^-] - (G[*] + G[CO_2] + 8\,G[H^+ + e^-]) \quad (S7)$$

$$\Delta G[*CH_3O] = G[*CH_3O] + G[H_2O] + 3 \times G[H^+ + e^-] - (G[*] + G[CO_2] + 8\,G[H^+ + e^-]) \quad (S8)$$

$$\Delta G[*CH_3OH] = G[*CH_3OH] + G[H_2O] + 2 \times G[H^+ + e^-] - (G[*] + G[CO_2] + 8\,G[H^+ + e^-]) \quad (S9)$$

$$\Delta G[*CH_3] = G[*CH_3] + 2 \times G[H_2O] + G[H^+ + e^-] - (G[*] + G[CO_2] + 8\,G[H^+ + e^-]) \quad (S10)$$

$$\Delta G[*+CH_4] = G[*] + G[CH_4] + 2 \times G[H_2O] - (G[*] + G[CO_2] + 8\,G[H^+ + e^-]) \quad (S11)$$

Where * is the substrate, U is the applied overpotential and e is the elementary charge. In this study, U=0V versus reversible hydrogen electrode is adopted.

The adsorption energy of CO_2 and the desorption energy of CO and CH_4 on the stoichiometric were calculated by the following equation:

$$E_{ads} = E_{CO2*} - E_{CO2} - E_* \quad (S12)$$

$$E_{des1} = E_{CO} + E_* - E_{CO*} \quad (S13)$$

$$E_{des2} = E_{CH4} + E_* - E_{CH4*} \quad (S14)$$

E_{CO2*}, E_{CO*} and E_{CH4*} is the total energy of sample absorbed with CO_2, CO and CH_4. E_{CO2} is the total energy of the optimized gas phase CO_2 molecule, E_* is the total energy of sample.

Band-gap energy (E_g) can be obtained by using UV−vis absorption spectra according to the formula

$$\alpha h\nu = A(h\nu - E_g)^{n/2} \quad \text{(S15)}$$

Where α is the absorption coefficient of material. *h* and *v* represent the Planck constant and frequency of the incident light, respectively. A is designated as a proportionality constant.

Calculation details

Table S1. Free energy (eV) for different samples in different states

	Vo-Fe-CoO	Fe-CoO	Vo-CoO	CoO
G[*]	-232.964	-241.000	-232.128	-236.976
G[*COOH]	-260.442	-268.132	-258.741	-261.714
G[*CO]	-249.785	-257.508	-247.703	-251.707
G[*CHO]	-252.494	-260.301	-250.565	-254.481
G[*CH_2O]	-256.645	-264.877	-253.226	-258.643
G[*CH_3O]	-261.106	-267.553	-259.177	-266.547
G[*CH_3OH]	-263.499	-271.838	-261.689	-266.547
G[*CH_3]	-253.541	-260.726	-251.733	-255.393
G[*CH_4]	-257.104	-266.108	-256.291	-261.628
G[*CO_2]	-256.902	-265.964	-254.952	-259.089

Table S2. Free energy (eV) for other species

Species	H2	H2O	CO2	CO	CH4
G (eV)	-6.89	-14.32	-23.33	-15.26	-23.44

Table S3. Free energy (eV) of CO_2 photoreduction for different samples

	Vo-Fe-CoO	Fe-CoO	Vo-CoO	CoO
ΔG [*+CO_2]	0	0	0	0
ΔG[*COOH]	-0.699	-0.351	0.167	2.043
ΔG[*CO]	-0.911	-1.304	0.335	1.179
ΔG[*CH*]	-0.171	0.060	0.923	1.823
ΔG*[CH_2O]	-0.872	-1.067	1.712	1.144
ΔG[*CH_3O]	-1.882	-0.293	-0.789	0.371
ΔG[*CH_3OH]	-0.825	-1.127	0.149	0.140
ΔG[*CH_3]	-1.737	-0.886	-0.765	0.423
ΔG [*CO_2]	-0.609	-1.634	0.505	1.217
ΔG[CO]	-1.56	-1.248	-0.414	0.529
ΔG[CH_4]	-0.700	-1.667	-0.723	-1.211

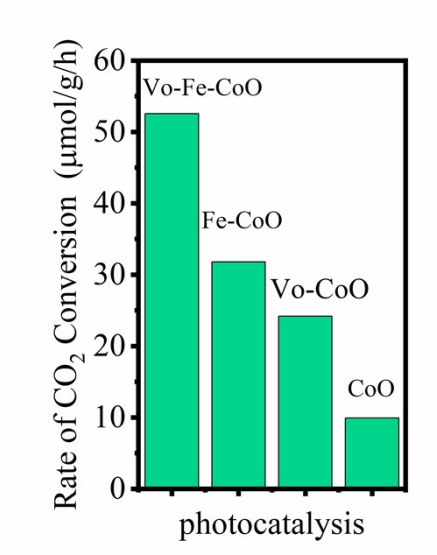

Fig. S2 Rate of CO_2 conversion for V_o-Fe-CoO, Fe-CoO, Vo-CoO and CoO single-unit-cell layers.

The oxygen evolution is estimated according to the principle of conservation of charge and the calculation method is as follows.

In Fig.6, the results of SVUV-PIMS identify that there are five kinds of gases (CO_2, CO, CH_4, O_2 and H_2O vapor) exist in the closed reactor. The reduction products are CO and CH_4, the O_2 is the oxidation product. Additionally, the reduction of CO_2 to CH_4 requires eight electrons, and reduction to CO needs two electrons. And the generation of O_2 corresponds to the four-electron process.[9] Consequently, the following reaction formula can be deduced.

$$2H_2O + 4h^+ \rightarrow 4H^+ + O_2\uparrow \quad \text{(S16)}$$

$$CO_2 + 2H^+ + 2e^- \rightarrow CO\uparrow + H_2O \quad \text{(S17)}$$

$$CO_2 + 8H^+ + 8e^- \rightarrow CH_4\uparrow + 2H_2O \quad \text{(S18)}$$

$$n(O_2) = 0.5*n(CO) + 2*n(CH_4) \quad \text{(S19)}$$

The rate of Gas (CO, CH_4 and O_2) production and the time-resolved O_2 production for V_o-Fe-CoO, Fe-CoO, Vo-CoO and CoO single-unit-cell layers are shown in Fig.S3 and Fig.S4.

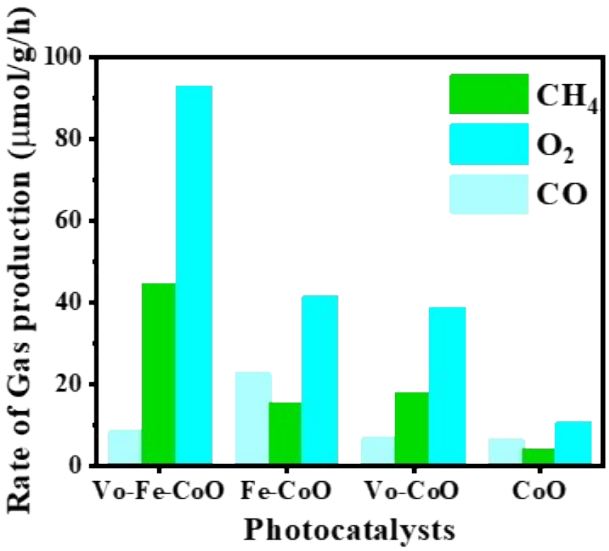

Fig. S3 Rate of gas production for V_o-Fe-CoO, Fe-CoO, V_o-CoO and CoO single-unit-cell layers.

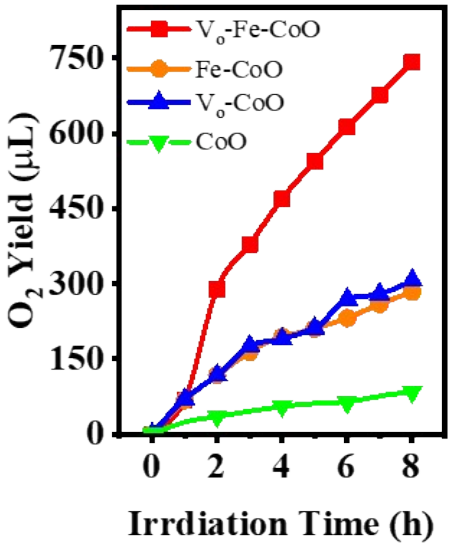

Fig. S4 Time-resolved O_2 production for V_o-Fe-CoO, Fe-CoO, Vo-CoO and CoO single-unit-cell layers.

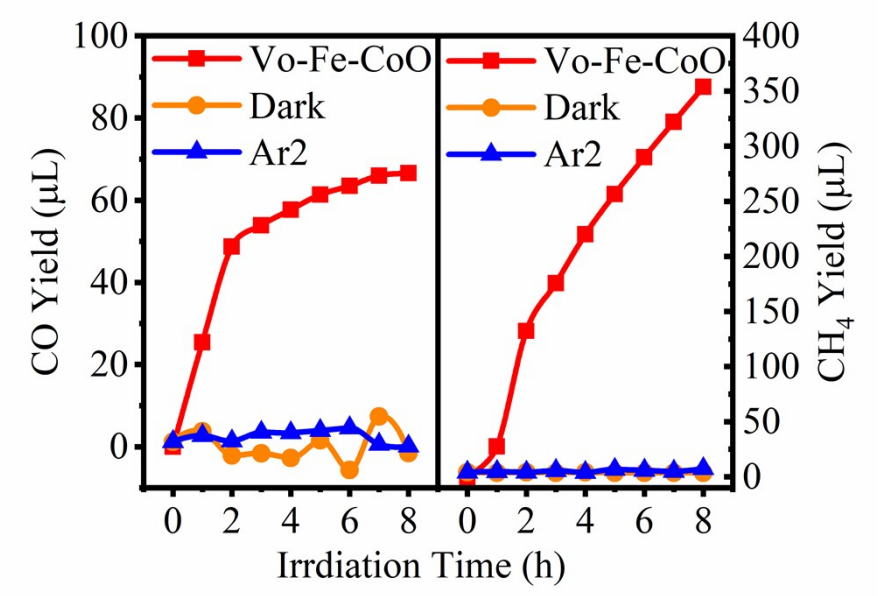

Fig. S5 Time-resolved CO (left) and CH_4 (right) productions for V_o-Fe-CoO under light radiation and CO_2 atmosphere, under dark and CO_2 atmosphere, under light radiation and Ar_2 atmosphere, respectively.

Table S4. Proportion of CH_4 in CO_2 reduction products

Samples	Vo-Fe-CoO	Fe-CoO	Vo-CoO	CoO
η (%)	91.40 %	57.02 %	84.00 %	54.95 %

$$\eta\ (\%)=R(CH_4) / [\ R(CH_4) + R(CO)] \times 100\ \% \quad (S20)$$

Where $R(CH_4)$, R(CO) denote the rate of methane and carbon monoxide evolution in the photocatalysis.

Table S5. Quantum efficiency of CO_2 reduction products

Samples	N (μmol)	QY (%)
Vo-Fe-CoO	370.40	0.38
Fe-CoO	164.59	0.17
Vo-CoO	153.42	0.16
CoO	42.41	0.05

The quantum efficiency is defined by the ratio of the effective electrons used for CO_2 reduction to the total input photon flux. The reduction of CO_2 molecules to CH_4 molecule requires eight electrons:

$$QY\ (\%) = \text{Number of reacted electrons/ number of incident photons} \times 100\% \quad (S21)$$

$$n = (2 \times \text{the number of CO}) + (8 \times \text{the number of } CH_4) \text{ molecules} \quad (S22)$$

$$\text{Number of reacted electrons} = n \times N_A \quad (S23)$$

$$\text{Number of incident photons} = \text{Light absorbed by the photocatalyst/ photon energy} \quad (S24)$$

$$\text{Light absorbed by the photocatalyst} = W \times A \times t \quad (S25)$$

$$\text{Photon energy} = h \times c/\lambda \quad (S26)$$

$$QY\ (\%) = n \times N_A \times h \times c/ (W \times A \times \lambda \times t) \quad (S27)$$

Where N_A is Avogadro's number (6.022×10^{23} mol^{-1}). h is Planck's constant ($h = 6.63 \times 10^{-34}$ J·s). c is the speed of light (3×10^{17} nm s^{-1}). t is irradiation time. W is simulated solar irradiation (230mW cm^{-2}). A is the geometric

irradiation area of the photocatalyst on the quartz fiber plate placed inside the reactor (28.26 cm^2).

Table S6. The position of CB and VB for samples (NHE, pH = 7).

Sample	V_o-Fe-CoO	Fe-CoO	V_o-CoO	CoO
CB	-0.59 eV	-0.64 eV	-0.67 eV	-0.68 eV
Eg	1.37 eV	1.46 eV	1.48 eV	1.51 eV
VB	0.78 eV	0.82 eV	0.81 eV	0.83 eV

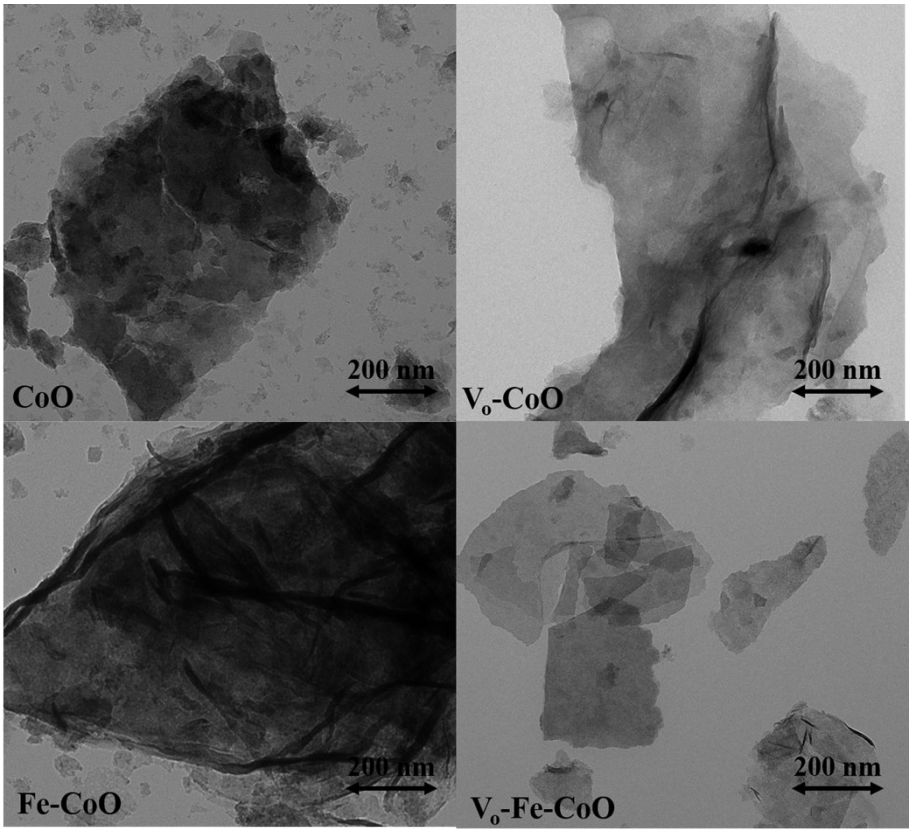

Fig. S6 TEM images of V_o-Fe-CoO, Fe-CoO, V_o-CoO and CoO single-unit-cell layers.

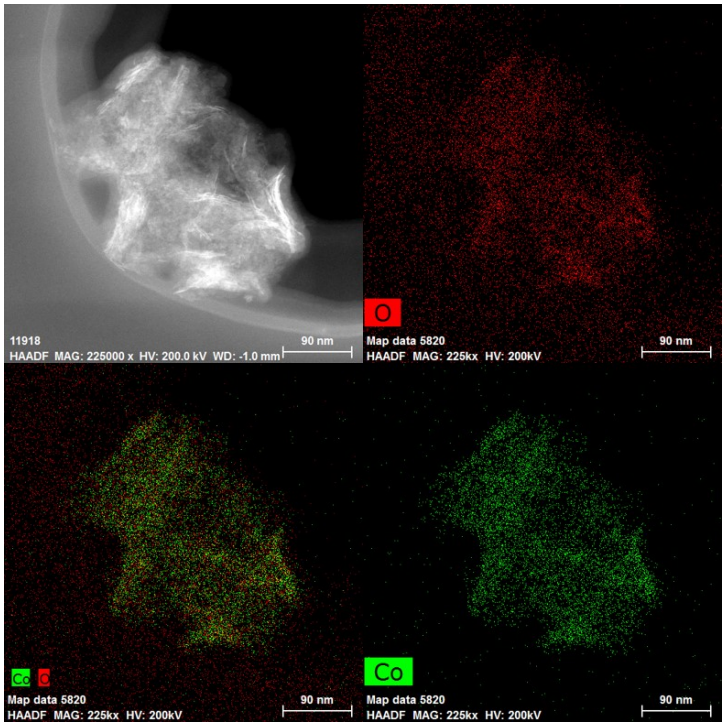

Fig. S7 HAADF-STEM and EELS mapping of CoO single-unit-cell layers.

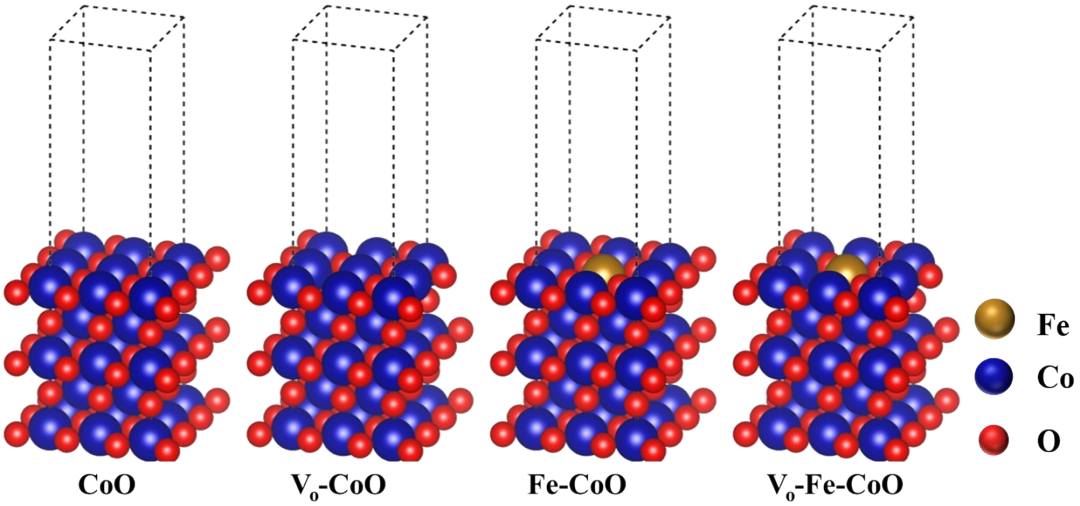

Fig. S8 Structural models of V_o-Fe-CoO, Fe-CoO, V_o-CoO and CoO single-unit-cell layers.

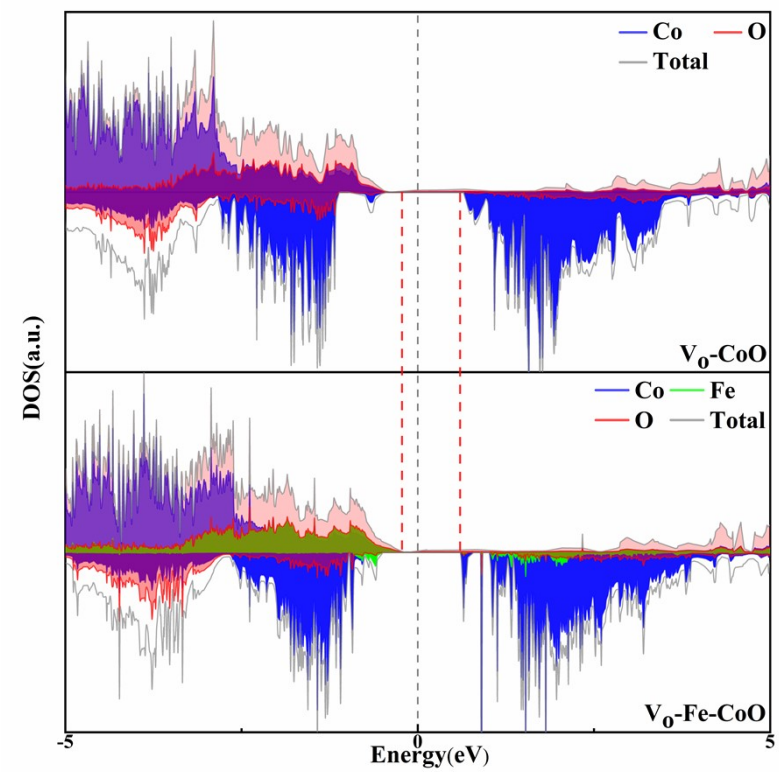

Fig. S9 Density of states (DOS) of V_o-Fe-CoO and V_o-CoO single-unit-cell layers.

1. X. Y. Pan, M. Q. Yang, X. Z. Fu, N. Zhang and Y. J. Xu, Defective TiO_2 with oxygen vacancies: synthesis,properties and photocatalytic applications, *Nanoscale* **2013**, 5, 3601-3614.
2. L. Iglesias, A. Sarantopoulos, C. Magen and F. Rivadulla, Oxygen vacancies in strained $SrTiO_3$ thin films: Formation enthalpy and manipulation, *Phys Rev B*, **2017**, 95, 1-7.
3. X. Guo, C. Zhong, D. Mao, W. Song, L. U and G. Hong, *RSC Adv.* **2015**, 5, 52958-52965.
4. W. Li, G. Zhang, X. Jiang, Y. Liu, J. Zhu, F. Ding, Z. Liu, X. Guo and C. Song, *ACS Ca*t. **2019**, 9, 2739–2751.
5. Y. B. Shi, G. M. Zhan, H. Li, X. B. Wang, X. F. Liu, L. J. Shi, K. Wei, C. C. Ling, Z. L. Li, H. Wang, C. L. Mao, X. Liu and L. Z. Zhang, *Adv Mater* **2021**, 0935-9648
6. L. Jiang, K. Wang, X. Wu and G. Zhang, *Solar RRL* **2020**, 5, 2000326.
7. P. E. Blochl, Phys. Rev. B,**1994**, 50, 17953.
8. J. P. Perdew, K. Burke, M. Ernzerhof, *Phys. Rev. Lett.*, **1996**, **77**, 3865.
9. X. D. Li, Y.F. Sun, J. Q. Xu, Y. J. Shao, J. Wu, X. L. Xu, Y. Pan, H.X. Ju, J. F. Zhu and Y. Xie, Nat. Energy, **2019**, 4(8).